COMMUNICATION

Check for updates

Surface-modified anode current collectors *via* lithiophilic zinc-based bimetallic co-electrodeposition for lithium–metal batteries

Dong Geun Kim, [ID] †[a] Dongyeon Won,†[ab] Inyeong Yang, [ID] [ac] Sukkyung Kang, [ID] [ad] Jae Young Seok, [ID] [e] Hyunwoong Baek[a] and Sanha Kim [ID] *[ad]

Lithium–metal batteries (LMBs) are considered promising next-generation energy storage systems due to their extremely high theoretical capacity and low electrochemical potential. However, their practical application is limited by the formation of lithium dendrites and poor interfacial stability during cycling. In this study, we propose a scalable CuZn bimetallic co-electrodeposition strategy for modification of current collector surfaces that effectively suppress dendritic growth and enhance cyclic reversibility. Zinc, a lithiophilic metal, was selected as a surface modifier owing to its favorable alloying characteristics with lithium. Substantial differences in standard reduction potentials exist between Cu and Zn, yet we successfully deposited Cu and Zn simultaneously by introducing potassium pyrophosphate into the electrolyte, which modulates the ion activity through complexation. The CuZn morphology was further tuned from flat films to branched nanostructures by controlling the electrolyte composition and deposition voltage. Post-deposition annealing facilitated interdiffusion at the Cu/CuZn interface, resulting in the formation of a recrystallized $Cu_{0.75}Zn_{0.25}$ alloy and improved mechanical bonding. Compared to bare Cu foils, the heat-treated CuZn current collectors extended the cell lifespan by 44.3% and the nanostructured CuZn further improved it by 87.2%. Electrochemical impedance spectroscopy and lithium nucleation overpotential analysis confirmed reduced interfacial resistance and improved uniformity in Li plating behavior. This work offers a practical and scalable approach for surface modification of anode current collectors for stable and long-life LMBs.

New concepts

We develop a one-step surface modification strategy for lithium–metal batteries by introducing lithiophilic zinc through bimetallic Cu–Zn co-electrodeposition. The key concept is the use of pyrophosphate to reduce the large reduction potential gap between Cu^{2+} and Zn^{2+}, enabling stable and simultaneous CuZn alloy co-deposition in a single aqueous bath. By tuning the concentrations of Cu^{2+}, Zn^{2+}, and pyrophosphate, as well as the applied voltage and deposition time, the morphology of the CuZn layer can be precisely controlled—from smooth films to high-surface-area branched nanostructures—without requiring sputtering, high-temperature alloying, or 3D microfabrication. This approach differs fundamentally from previous strategies, which relied on multi-step coatings or complex thermal/structural processing to achieve lithiophilicity and controlled surface architectures. Our single-step electrochemical route simultaneously optimizes both the chemical (zinc-induced lithiophilicity) and structural (surface area and branch density) characteristics of the current collector, while maintaining compatibility with large-area and roll-to-roll manufacturing. Furthermore, post-annealing of the co-deposited CuZn layer enhances interfacial adhesion through alloy interdiffusion, and nanostructuring further increases active surface area. These combined effects significantly improve cycling stability by promoting uniform Li nucleation and suppressing dendritic growth. Overall, this concept provides a new pathway for designing durable and dendrite-resistant anode current collectors for next-generation lithium–metal batteries.

1. Introduction

The demand for high-performance batteries is increasing significantly as electrification and automation accelerate across diverse industrial sectors. Although lithium-ion batteries (LIBs) have dominated the market for decades, their reliance on graphite anodes with a limited theoretical capacity of 372 mAh g^{-1} poses a bottleneck for further energy density improvements. This limitation necessitates the development of next-generation battery technologies. Lithium metal (Li-metal) has been proposed as a promising anode material due to its ultra-low electrochemical potential (-3.04 V *vs.* standard hydrogen electrode (SHE)) and exceptionally high theoretical capacity of 3860 mAh g^{-1}, almost ten times that of graphite.[1] However, lithium–metal batteries

[a] *Department of Mechanical Engineering, Korea Advanced Institute of Science and Technology, Daejeon, 34141, Republic of Korea. E-mail: sanhkim@kaist.ac.kr*
[b] *Future Tech. Center, LG Energy Solution, Seoul, 07796, Republic of Korea*
[c] *R&D Division, Hyundai Motor Company, Uiwang, 16082, Republic of Korea*
[d] *KAIST InnoCORE PRISM-AI Center, Korea Advanced Institute of Science and Technology, Daejeon, 34141, Republic of Korea*
[e] *Department of Mechanical System Design Engineering, Seoul National University of Science and Technology, Seoul, 01811, Republic of Korea*
† These authors contributed equally.

(LMBs) have not yet commercialized, primarily due to the concerns regarding their limited cycle life and safety. The principal challenge is the formation of lithium dendrites during repeated charge–discharge cycles at the anode, which not only destabilizes the solid electrolyte interphase (SEI) but also accelerates electrolyte depletion.[2] Moreover, the mechanical fragility of these dendrites leads to the formation of electrically isolated "dead Li", one of the main causes of capacity loss. In severe cases, dendrites may pierce the separator and cause internal short circuits, potentially resulting in thermal runaway or explosion.[3]

To suppress dendrite growth in lithium–metal batteries, diverse strategies have been proposed. At the cell level, advanced electrolytes incorporating functional additives have been developed to form stable solid electrolyte interphases (SEI), effectively reducing side reactions and promoting uniform lithium deposition.[4] In parallel, novel separator architectures have been introduced to modulate ion flux and inhibit dendritic propagation.[5] In addition, electrolyte composition plays a crucial role in controlling dendrite growth, as solvent viscosity and Li+ transport properties strongly influence current distribution at the electrode interface.[6] Recent studies have shown that highly concentrated electrolytes and fluorinated diluents can effectively stabilize the interfacial chemistry and promote the formation of uniform SEI layers, thereby enhancing lithium reversibility and cycling stability.[7,8]

Beyond electrolyte and separator engineering, structural innovation of the current collectors (CCs) has emerged as a critical approach. Recent studies emphasize the importance of lithiophilic surface design and engineered morphologies to stabilize lithium nucleation and growth.[9,10] In particular, the introduction of lithiophilic metals such as zinc (Zn), which exhibit high affinity for lithium and lower nucleation overpotentials, has been shown to significantly enhance the lithium plating uniformity.[11,12] Building upon these principles, Wang et al. examined the fundamental behaviors at the Li–Cu interface, highlighting the benefits of surface coatings and 3D structuring in suppressing dendrite formation.[13] Gong et al. developed a carbon nanotube-based current collector with gradient lithiophilicity, enabling mechanically robust and

dendrite-free operation under lean-lithium conditions.[14] Huh et al. demonstrated a laser-assisted fabrication of crystallographically oriented 3D Cu collectors, achieving selective lithiophilicity and improved lithium plating behavior.[15] Gradient ion regulation strategies were also implemented by Zhang et al., who designed current collectors that could actively guide uniform lithium deposition.[16] Yang et al. suppressed dendrite formation by mitigating current concentration through nano–microstructural design of the current collector.[17] Lastly, Li et al. introduced metalized plastic current collectors reinforced with halloysite nanotubes and dual copper layers, balancing mechanical durability, energy density, and safety.[18]

The progress in CCs has been explored further toward three-dimensional structuring with enlarged surface areas to distribute the local current densities more evenly and suppress dendritic growth.[19,20] According to Sand's time equation, lowering the effective current density at the anode surface is an ideal strategy for delaying dendrite formation.[21] Accordingly, the combination of lithiophilic and high-surface-area current collectors has shown promise in extending the lifespan of LMBs. However, their practical implementation remains limited. One major obstacle is the scalability of current fabrication techniques. For instance, metal sintering or sputtering to coat zinc onto copper substrates requires prolonged processing times and is difficult to integrate into roll-to-roll manufacturing platforms used in large-scale battery production.[22,23] Another inherent limitation lies in the simplistic strategy of merely increasing lithiophilicity or surface area. Excessive volume changes during alloying between Li and lithiophilic metals can degrade the cycling stability,[24] and excessive porosity may lead to excessive SEI formation or accelerated galvanic corrosion, ultimately reducing energy density due to inactive volume expansion.

In this study, we propose a scalable and facile fabrication method for advanced current collectors via one-step CuZn co-electrodeposition. As illustrated in Fig. 1, the strategy aims to suppress the dendritic Li growth commonly observed on bare Cu foil anode current collectors by modifying their surface with a CuZn alloy layer. The incorporation of lithiophilic Zn enables

Fig. 1 Surface modification of Cu current collectors via bimetallic co-electrodeposition. Schematics of surface modification by simultaneous co-electrodeposition of Cu and Zn for prevention of dendritic Li growth. The co-electrodeposited CuZn morphology can be further tuned from a film to a nanobranch structure, enabling more stabilized Li growth during the charge–discharge cycling of LMBs.

more uniform and stabilized Li deposition. This method allows the simultaneous electrochemical deposition of Cu^{2+} and Zn^{2+} ions onto a Cu foil within a single aqueous bath. Potassium pyrophosphate is introduced as a complexing agent to tune the reduction behavior of Cu^{2+} and Zn^{2+}, thereby ensuring stable and uniform co-deposition. The resulting CuZn layers exhibit tunable composition and morphology, ranging from smooth alloy films to branched nanostructures with enlarged surface area. Post-annealing further promotes interdiffusion and recrystallization at the Cu/CuZn interface, enhancing mechanical adhesion and improving interfacial stability. Owing to these structural and chemical advantages, the optimized CuZn current collectors demonstrate significantly enhanced cycling stability, reduced interfacial resistance, and more uniform lithium plating compared with bare Cu. Overall, this work presents a single-step surface engineering strategy that offers a practical route toward stable and long-life lithium metal batteries.

2. Experimental

2.1 Co-electrodeposition and thermal annealing of CuZn

We simultaneously deposited Cu and Zn on Cu current collector surfaces in an electrolyte bath using a two-electrode configuration (Fig. 2). A 9-μm-thick copper foil (MTI Corp.) was used as the working electrode, and a brass mesh (Cu:Zn = 65:35) served as the counter electrode. Prior to the electrodeposition, the copper foil was immersed in 1 M H_2SO_4 for 30 minutes to remove surface oxides, rinsed with deionized (DI) water, and dried with nitrogen gas. The brass mesh was cleaned in acetone

for 1 minute and similarly dried with nitrogen. A polycarbonate (PC) jig with a 6-cm-diameter opening was applied to define a controlled circular deposition area. The jig was designed to shield one side of the copper foil, ensuring deposition occurred only on the exposed surface. The foil and mesh were fixed onto the jig using copper adhesive tape and electrically connected to a power supply, with the brass mesh serving as the anode and the copper foil as the cathode. The electrolyte solution consisted of 300 mL of DI water with sequential addition of potassium pyrophosphate ($K_4P_2O_7$), copper sulfate ($CuSO_4$), and zinc sulfate ($ZnSO_4$). After all salts were added, the solution was stirred at 1000 rpm for 30 minutes at room temperature to ensure full dissolution. Different solution compositions and deposition conditions were prepared to study the influence of Cu:Zn ratios on deposition morphology and electrochemical performance. Electrodeposition was carried out by adjusting voltage and time according to each condition. Upon completion of deposition, the CuZn coated copper foils were rinsed with DI water to remove residual electrolyte and dried under vacuum. The electrodes were then cut into disc shapes using a precision disk cutter (MSK-T110, MTI Corp.) and stored in an argon-filled glovebox (WGB 1500, Woosung Highvac) with O_2 and H_2O levels maintained below 1 ppm.

To improve the mechanical integrity and electrochemical stability of the electrodeposited CuZn layer with the Cu current collector, we conducted thermal annealing. The co-deposited layer tends to delaminate during cycling without such thermal treatment. In such cases, internal residual stresses may lead to non-uniform lithium plating, thereby degrading battery performance. Post-annealing enhances the adhesion between the CuZn layer and the underlying Cu foil and improves the
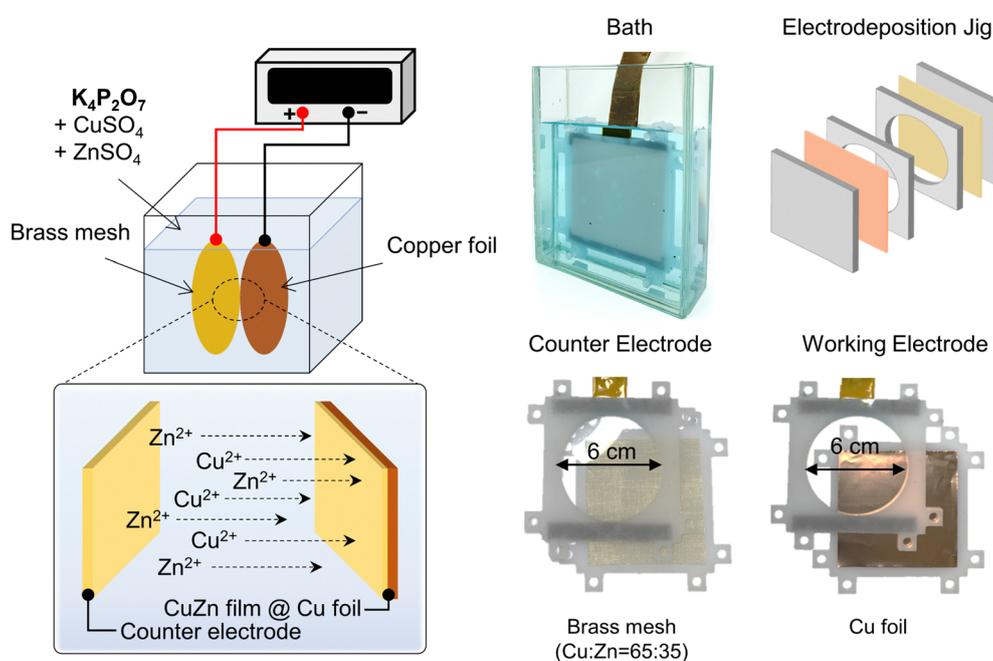

Fig. 2 CuZn co-electrodeposition on a Cu current collector in a two-electrode system. A custom-designed 6 cm diameter polycarbonate jig enables controlled one-sided deposition on bare Cu foils, while a pyrophosphate-based electrolyte allows simultaneous co-deposition of Cu^{2+} and Zn^{2+}.

uniformity of bimetallic crystalline structures. The annealing was conducted in a vacuum furnace (Samheung Energy, SH-FU-120TG) with the CuZn coated foils placed on quartz plates. The chamber was evacuated using a vacuum pump and purged with argon at a flow rate of 5 SLPM. The temperature was ramped up to 300 °C over 1 hour and held for an additional 2 hours under vacuum to complete the thermal treatment.

2.2 Morphological and compositional analysis of co-electrodeposited CuZn

The micro-/nano-scale surface morphology of the current collectors plays a critical role in determining the deposition behavior of lithium, as it directly influences the nucleation and growth dynamics.[24,25] Accordingly, we systematically investigated the surface of CuZn deposits formed under various co-electrodeposition conditions. The deposition parameters were controlled by adjusting the applied voltage and the concentrations of potassium pyrophosphate ($K_4P_2O_7$), copper sulfate ($CuSO_4$), and zinc sulfate ($ZnSO_4$) in the electrolyte. Surface morphologies were characterized using scanning electron microscopy (SEM, SU5000, Hitachi, Japan) at an accelerating voltage of 10 kV. In addition, the structural characteristics of the CuZn deposits were quantitatively evaluated using AFM-based surface roughness (S_q), SEM (50° tilting) for measuring nanobranch length, and binary image analysis with ImageJ[26] to quantify the nanostructure density.

The CuZn composition at the current collector surface is also a crucial determinant of both mechanical and chemical stability, which in turn affects the electrochemical performance of LMBs. Excessive Zn content can lead to substantial volumetric expansion due to Li–Zn alloy formation, potentially causing cracking or delamination of the co-deposited layer.[1] Conversely, insufficient Zn content may compromise the stability of lithium deposition and negatively affect battery performance. To address these concerns, the relative concentrations of $CuSO_4$ and $ZnSO_4$ in the electrolyte were varied to evaluate the tunability of CuZn composition via co-electrodeposition. The elemental composition of the deposited layers was analyzed by energy-dispersive X-ray spectroscopy (EDS, Octane Elite 25, EDAX).

For cross-sectional analysis of the CuZn layer, transmission electron microscopy (TEM, Tecnai F20, Thermo Fisher Scientific) was performed. TEM lamellae were prepared using focused ion beam (FIB) milling (Helios Nanolab 450 F1, FEI Company). The crystalline structure of the CuZn deposits was further characterized via X-ray diffraction (XRD, SmartLab, RIGAKU). To isolate the signal from the thin ($\sim$300 nm) co-deposited layer and exclude contributions from the underlying Cu foil, grazing incidence X-ray diffraction (GIXRD) was employed.

2.3 Electrochemical characterization of CuZn current collectors

To evaluate the electrochemical performance of the co-electrodeposited CuZn CCs in LMB configurations, a series of cell-level tests were conducted. The CuZn CCs were assembled into coin cells (CR2032, MTI) using a lithium chip (250 μm

thick, MTI) and a Celgard 2325 separator. For comparison, both half (Li‖Cu) and full cells were prepared. The electrolyte consisted of 1.0 M LiPF6 dissolved in a mixture of ethylene carbonate (EC) and diethyl carbonate (DEC) (1 : 1 by volume, Dongwha Electrolyte), with 10 wt% fluoroethylene carbonate (FEC) and 1 wt% vinylene carbonate (VC). A total of 75 μL of the electrolyte was used per cell. The CuZn current collectors were punched into 19-mm-diameter discs, while lithium metal chips were cut into 16-mm-diameter discs. All coin cells were sealed using a hydraulic crimper (MSK-110, MTI Corp.) under an applied pressure of 6.9 MPa.

Electrochemical impedance spectroscopy (EIS) was performed using an Ivium-n-stat potentiostat (Ivium Technologies) with a frequency range of 10^{-3}–10^5 Hz, an amplitude of 50 mV, and an equilibration time of 1000 seconds prior to measurement. Voltage profiles, cycling stability, and coulombic efficiency (CE) were assessed using a battery cycler (WBCS3200L, WonATech). Prior to long-term cycling, all Li‖Cu and Li‖CuZn cells underwent five initial formation cycles at a current of 50 μA within a voltage range of 0–1 V to stabilize the electrode–electrolyte interface.

3. Results and discussion

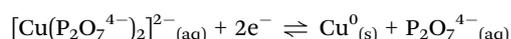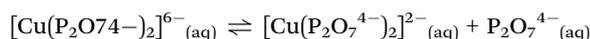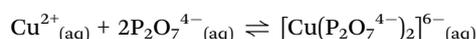## 3.1 One-step CuZn bimetallic electrodeposition

We selected zinc (Zn) as the lithiophilic element to modify the surface characteristics of the anode current collector due to its favorable properties for stabilizing lithium (Li) deposition. Among various lithiophilic candidates, Zn offers a relatively low volumetric expansion upon alloying with lithium ($\sim$71%). In addition, its high natural abundance and low cost make Zn a practical and scalable choice for surface engineering of current collectors.[27] However, electrodeposition of Cu and Zn in a single step presents fundamental challenges due to the large disparity in their standard reduction potentials ($E°Cu$ = +0.34 V, $E°Zn$ = −0.76 V vs. SHE). Accordingly, the reduction of Cu^{2+} during the deposition occurs much faster than that of Zn^{2+}, thereby hindering balanced bi-material deposition. This imbalance arises not only from the thermodynamic potential difference but also from the disparity in reduction kinetics between Cu^{2+} and Zn^{2+}. The faster nucleation and growth of Cu lead to preferential Cu-rich deposition, thereby suppressing competitive Zn incorporation under identical applied potentials.

To achieve a uniform CuZn alloy in a single electrodeposition step, we employed a complexing agent that aligns the reduction potentials of Cu^{2+} and Zn^{2+}. Complexing agents are commonly employed to regulate their ionic activity to match the reduction potentials of Cu^{2+} and Zn^{2+}. A number of complexing agents have been explored to mediate Cu^{2+} ion activity, including ethylenediaminetetraacetic acid (EDTA),[28] triethanolamine (TEA),[29] ammonium sulfate,[30] cetyltrimethylammonium bromide (CTAB),[31] and citrate.[32] Among these, we chose pyrophosphate, which has proven to be especially effective for CuZn co-deposition. Pyrophosphate not only forms stable complexes with Cu^{2+} but also inhibits the formation of metal

hydroxides, thereby enabling uniform and compact deposits.[33,34] Moreover, it is non-toxic and environmentally benign, further supporting its industrial applicability. It should be emphasized that the introduction of pyrophosphate is not intended merely to increase the Zn fraction in the CuZn layer. Simply increasing the $ZnSO_4$ concentration without regulating Cu reduction kinetics may result in unstable deposition behavior and poor compositional control. In contrast, pyrophosphate selectively suppresses Cu^{2+} reduction *via* complexation, enabling controlled co-deposition under the same applied potential.

Accordingly, a co-deposition bath comprising potassium pyrophosphate ($K_4P_2O_7$), copper(II) sulfate ($CuSO_4$), and zinc(II) sulfate ($ZnSO_4$) was used for co-deposition of Cu and Zn by single-step electrodeposition. The following equilibria describe the complexation of Cu^{2+} with pyrophosphate and the corresponding shift in its reduction potential:

$$Cu^{2+}_{(aq)} + 2P_2O_7^{4-}_{(aq)} \rightleftharpoons [Cu(P_2O_7^{4-})_2]^{6-}_{(aq)}$$

$$[Cu(P_2O74-)_2]^{6-}_{(aq)} \rightleftharpoons [Cu(P_2O_7^{4-})_2]^{2-}_{(aq)} + P_2O_7^{4-}_{(aq)}$$

$$[Cu(P_2O_7^{4-})_2]^{2-}_{(aq)} + 2e^- \rightleftharpoons Cu^0_{(s)} + P_2O_7^{4-}_{(aq)}$$

Through this mechanism, pyrophosphate induces a cathodic shift in the reduction potential of Cu^{2+} by modifying its electronic environment. As illustrated in Fig. 3a, the reduction potential of Cu^{2+} is significantly shifted toward more negative values upon pyrophosphate complexation, narrowing the electrochemical gap with Zn^{2+} and enabling simultaneous co-deposition. This alignment of Cu^{2+} and Zn^{2+} reduction potentials facilitates stable and uniform co-deposition within a single bath, enabling precise control over CuZn alloy composition and morphology. This bimetallic electrodeposition method may exhibit simplicity, low cost, and compatibility with roll-to-roll processing over vapor-phase or chemical methods, which are widely adopted in battery manufacturing.

We confirmed that the formation of the $[Cu(P_2O_7)_2]^{6-}$ complex in the presence of pyrophosphate lowers the reduction potential of Cu (*vs.* SHE), thereby narrowing the potential gap between Cu^{2+} and Zn^{2+} and enabling the simultaneous co-deposition of a CuZn alloy. For the samples presented in Fig. 3b–d, electrodeposition was conducted at an applied voltage of 2.0 V for 1 min. These conditions were selected to minimize mass-transport limitations and to clearly isolate the intrinsic effect of pyrophosphate complexation on alloy composition and surface morphology. The influence of pyrophosphate on the surface morphology of CuZn deposits prepared from the $Cu_{10}Zn_{40}$ electrolyte is shown in Fig. 3b. Without pyrophosphate, the deposited layer exhibits irregular and coarse surface features, reflecting kinetically dominated Cu growth. Upon the addition of 100 mM pyrophosphate, the surface becomes noticeably more homogeneous and compact, indicating moderated Cu nucleation and improved compositional balance during deposition. The surface roughness exhibited clear dependence on electrolyte composition and pyrophosphate concentration. Under pyrophosphate (PP)-free conditions ($Cu_{10}Zn_{40}$, PP 0 mM, 2 V), S_q reached 545.5 nm, representing the roughest surface, whereas the addition of 100 mM pyrophosphate significantly reduced S_q to 112.7 nm. This reduction is attributed to the complexation of Cu^{2+} and Zn^{2+} by pyrophosphate ligands, which promotes more uniform alloy growth and results in a smoother film-like morphology.

To experimentally examine the influence of pyrophosphate on the actual deposition composition, the elemental distribution of Cu and Zn was analyzed using EDS mapping. In the $Cu_{10}Zn_{40}$ electrolyte without pyrophosphate, a Cu-rich film was formed due to preferential Cu deposition. Although Zn was detected at nearly 50 at% under this condition, the applied overpotential (2.0 V) is sufficiently negative to drive Zn^{2+} reduction once initial Cu nuclei are formed on the bare Cu substrate. However, due to the intrinsically faster reduction kinetics of Cu^{2+}, the overall morphology remains Cu-dominant. In contrast, when pyrophosphate (100 mM) was added to the
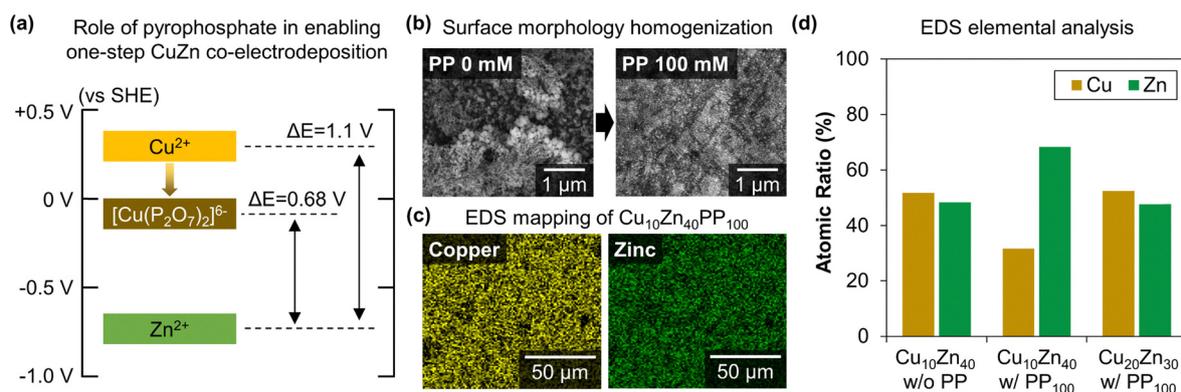
Fig. 3 Pyrophosphate complexation on CuZn reduction behavior and alloy co-deposition. (a) Reduction potential shift of Cu^{2+} and Zn^{2+} induced by pyrophosphate complexation, enabling simultaneous alloy co-deposition. (b) Surface morphology of $Cu_{10}Zn_{40}$ deposits without and with the addition of pyrophosphate (0 mM PP *vs.* 100 mM PP), showing improved morphological homogeneity upon PP addition. (c) EDS elemental mapping of Cu and Zn deposited from the $Cu_{10}Zn_{40}$ electrolyte with pyrophosphate (100 mM). (d) Atomic composition of co-electrodeposited CuZn films prepared from $Cu_{10}Zn_{40}$ without pyrophosphate, $Cu_{10}Zn_{40}$ with 100 mM pyrophosphate, and $Cu_{20}Zn_{30}$ with 100 mM pyrophosphate.

same electrolyte, Zn deposition increased markedly, resulting in a more uniform CuZn alloy layer (Fig. 3c). As shown in Fig. 3d, the atomic composition of the electrodeposited films shifts distinctly from Cu-rich to Zn-rich upon the introduction of pyrophosphate. This transition is attributed to the strong complexation of pyrophosphate with Cu^{2+}, which reduces the concentration of free Cu^{2+} and suppresses its reduction kinetics, thereby increasing the relative contribution of Zn deposition. When the Cu concentration was increased by 10 mM and the Zn concentration was decreased by 10 mM under 100 mM pyrophosphate conditions, the Zn atomic fraction in the co-deposited layer decreased by approximately 20 at%, as determined by EDS analysis.

### 3.2 Surface morphology and properties of co-electrodeposited CuZn current collectors

In CuZn co-electrodeposition, the controllable processing parameters include applied voltage, the Cu^{2+}/Zn^{2+} ratio in the electrolyte, pyrophosphate concentration, and deposition time. We summarize how the morphology, surface roughness, and deposition density of CuZn films can be precisely controlled by tuning the applied voltage, Cu^{2+}/Zn^{2+} ratio, and pyrophosphate concentration in Fig. 4a. This compositional tunability is critical for optimizing both the lithiophilicity and mechanical integrity of the current collector for lithium metal battery applications.

The micro-/nano-scale surface morphology of the CuZn deposits was significantly influenced by the pyrophosphate concentration. As shown in Fig. 4b, at low pyrophosphate concentrations, sufficient ion supply promotes film-type deposition rather than branched growth. However, when sufficient pyrophosphate is introduced, complexation reduces the activity of free Cu^{2+} ions, and under elevated overpotential conditions, a local ion depletion zone forms near the electrode surface. As a result, limited ion supply leads to needle-like and branched CuZn growth. Under the 3 V and 2 min deposition conditions, a continuous film was formed at 100 mM PP concentration. When the PP concentration was increased to 400 mM, the surface became more granular. At 800 mM PP concentration, nanoscale branched structures were clearly observed. This behavior suggests a transition in the deposition mechanism influenced by ion depletion and nucleation dynamics.

A similar change in structural shape was observed under different applied voltage conditions. At a low pyrophosphate concentration (100 mM), a sufficient free metal ion concentration favored uniform deposition. In contrast, under high PP conditions (800 mM), the morphology strongly depended on applied voltage. At 2.0 V, the CuZn layer remained continuous. At higher voltages (≥ 3.0 V), enhanced ion depletion near the electrode surface led to branched growth. This phenomenon is attributed to the formation and expansion of an ion depletion layer at the electrode interface.[35] As the deposition voltage increased, this depletion zone widened, resulting in thinner and more vertically elongated dendritic branches.

To induce film morphology, 10 mM Cu, 40 mM Zn, 100 mM PP and 2 V were applied. To induce branched morphology, 10 mM Cu, 40 mM Zn, 800 mM PP and voltages above 3 V were employed. Fig. 4c–k present the SEM images of CuZn deposits obtained by systematically varying voltage, deposition time, and PP concentration to induce either film or branched
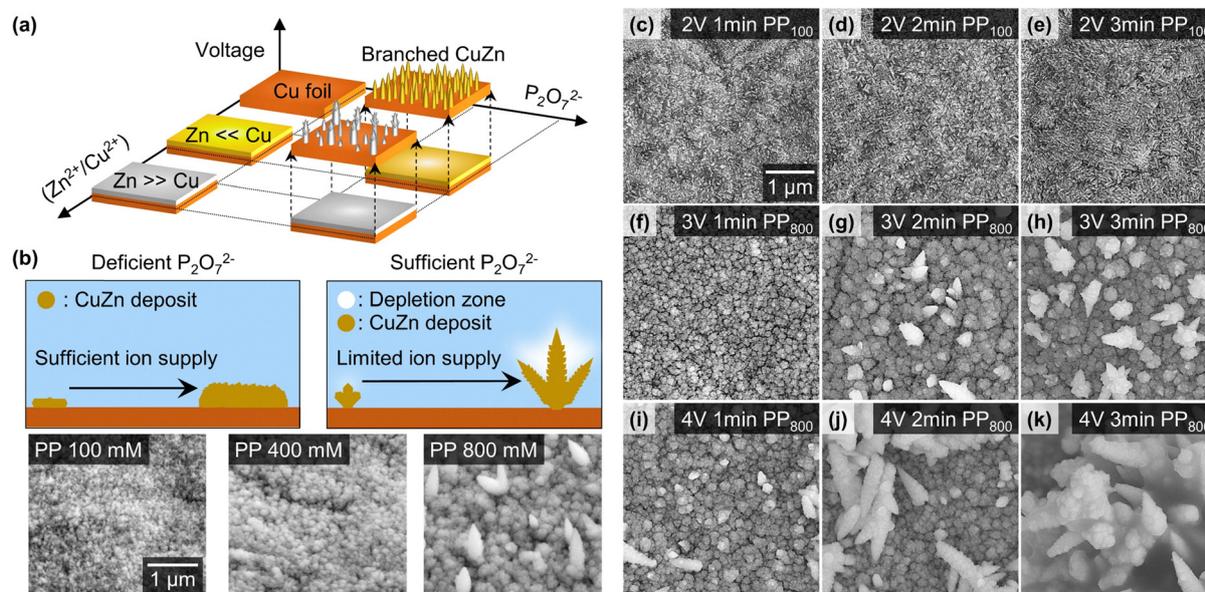
Fig. 4 Surface morphology and growth mechanism of CuZn deposits controlled by deposition parameters. (a) Schematic illustration of CuZn deposition regulated by applied voltage, Cu^{2+}/Zn^{2+} ratio, and pyrophosphate concentration. (b) Mechanism of film or branched CuZn growth as a function of pyrophosphate concentration, with the corresponding SEM images. (c)–(e) SEM images of CuZn deposited at 2 V under 100 mM PP for 1, 2, and 3 min, respectively. (f)–(h) SEM images of CuZn deposited at 3 V under 800 mM PP for 1, 2, and 3 min, respectively. (i)–(k) SEM images of CuZn deposited at 4 V under 800 mM PP for 1, 2, and 3 min, respectively.

structures. At 2 V and 100 mM PP, film-type CuZn deposition was consistently observed regardless of deposition time, with no significant morphological transition (Fig. 4c–e). Under 3 V and 800 mM PP, a more granular morphology was observed at 1 min (Fig. 4f), and nano-scale branched structures began to form after 2 min (Fig. 4g and h). Under 4 V and 800 mM PP, 1 min deposition produced larger granular features with a limited number of branches (Fig. 4i). Increasing the deposition time to 2 min resulted in pronounced branch formation with significantly increased size (Fig. 4j). At 3 min, excessive vertical growth led to micron-scale dendritic structures rather than well-defined nano-branches (Fig. 4k).

These results demonstrate that the morphology of the CuZn deposits—including surface roughness, branching geometry, and structural density—can be finely tuned to adjust both the surface area and mechanical robustness of the current collector. By optimizing the geometric features and chemical composition suitable for lithium–metal battery anodes, this approach provides a versatile surface-engineering strategy in which the CuZn structure can be systematically tailored through control of electrolyte ion concentration, applied voltage, and deposition time.

3.3 Surface modification of CuZn anode current collectors *via* thermal treatment

During the electrodeposition of CuZn onto the Cu foil, an interfacial region is formed between the two metals, which can lead to weak mechanical adhesion and degradation of long-term cycling stability. Therefore, a post-treatment process is required to reinforce the interfacial strength and improve the mechanical integrity of the current collector. Surface modification of the anode current collector with lithiophilic zinc in the form of a CuZn film is expected to improve the cycle life of LMBs, yet this improvement can be maximized after thermal treatment, which reinforces the mechanical integrity of the interface. For verification, the electrodeposited CuZn layer was first uniformly deposited to a thickness of approximately 300 nm on the surface of the 9 μm thick Cu foil, Fig. 5a. The energy-dispersive spectroscopy confirmed that the electrodeposited CuZn layer was Zn-rich compared to Cu. Notably, the deposited layer remained strictly on the surface without any penetration into the Cu foil. Following thermal treatment, however, significant microstructural changes were observed. The CuZn layer and the underlying Cu foil underwent recrystallization, during which Zn atoms diffused into the Cu substrate, forming new grain boundaries at the interface. This interdiffusion is expected to enhance mechanical integrity by eliminating interfacial delamination and promoting structural continuity between the layers. Grazing-incidence X-ray diffraction (GIXRD) results (Fig. 5b) support the interdiffusion during thermal annealing. Prior to annealing, characteristic peaks corresponding to the Zn-rich intermetallic phase Cu_5Zn_8 were observed. After annealing, the dominant phase transitioned to $Cu_{0.75}Zn_{0.25}$, indicating Zn diffusion into the bulk Cu. This compositional shift strongly suggests that thermal treatment improved metallurgical bonding at the CuZn–Cu interface.

The enhanced crystallographic stability of the electrodeposited CuZn layer after post-annealing was reflected in the cycling performance of Li‖Cu half cells. Galvanostatic charge–discharge (GCD) tests were conducted on Cu foil, CuZn, and heat-treated CuZn (CuZn HT) at current densities of 0.5, 1, and 2 mA cm^{-2} with a fixed areal capacity of 1 mAh cm^{-2}, as shown in Fig. 5c. At 0.5 mA cm^{-2}, compared to the bare Cu foil cell with a lifespan of 280 h, the Li‖CuZn cell demonstrated an extended lifespan of 335 h. This improvement is attributed to the incorporation of Zn, a more lithiophilic metal, which enhances lithium affinity and promotes more uniform Li plating. After post-annealing, the Li‖CuZn HT cell exhibited a further improved lifespan of 404 h, confirming the beneficial effect of recrystallization and interfacial diffusion on cycling stability. Under more rigorous conditions, at 1 mA cm^{-2}, the lifespans were 160 h for Cu foil, 270 h for CuZn, and 350 h for CuZn HT. At 2 mA cm^{-2}, the corresponding lifespans were 70 h (Cu foil), 120 h (CuZn), and 240 h (CuZn HT), respectively. These results clearly demonstrate the superior cycling stability of CuZn and CuZn HT compared to bare Cu, particularly under high-current conditions. Coulombic efficiency (CE) trends further corroborated these findings, as shown in Fig. 5d. The average number of cycles at which CE fell below 80% increased from 48 cycles for the Li‖Cu cell to 70 cycles for the Li‖CuZn cell, and further to 84 cycles for the Li‖CuZn HT cell. These results indicate improved Li reversibility and reduced parasitic reactions upon surface modification and subsequent thermal treatment.

We further investigated the Li deposition behavior during electrochemical cycling to verify the advantage of the lithiophilic bi-metal surface. Li‖CuZn cells with a 16 mm effective diameter were first subjected to five formation cycles at 50 μA within 0–1 V, followed by Li deposition at 0.5 mA cm^{-2} with an areal capacity of 1 mAh cm^{-2}. Li plating was examined after the 1st and 50th deposition cycles on Cu foil and CuZn HT current collectors using SEM (SU5000, Hitachi), as shown in Fig. 5e. On the bare Cu foil, Li was deposited in an irregular and dendritic manner, whereas on the CuZn HT surface, Li deposition was more conformal and uniform. Both the 1st and 50th Li plating cycles exhibited uniform deposition on the CuZn HT current collector, indicating that the lithiophilicity of the modified interface was maintained even after prolonged cycling. Such morphological uniformity is essential for suppressing localized current density spikes, which are known to trigger dendritic growth and eventual cell failure.

3.4 Nanoengineering *via* CuZn co-electrodeposition

We further promoted the formation of branch-like morphologies to investigate the synergistic effect of structural design and bi-metal surface composition. To examine the influence of the Cu^{2+}/Zn^{2+} ionic concentration ratio in the electrolyte on electrochemical performance, two electrolyte compositions, $Cu_{20}Zn_{30}$ and $Cu_{10}Zn_{40}$, were used to deposit nano-CuZn films. Both were fabricated under identical electrodeposition parameters (800 mM PP, 3 V, and 2 min) to ensure a fair
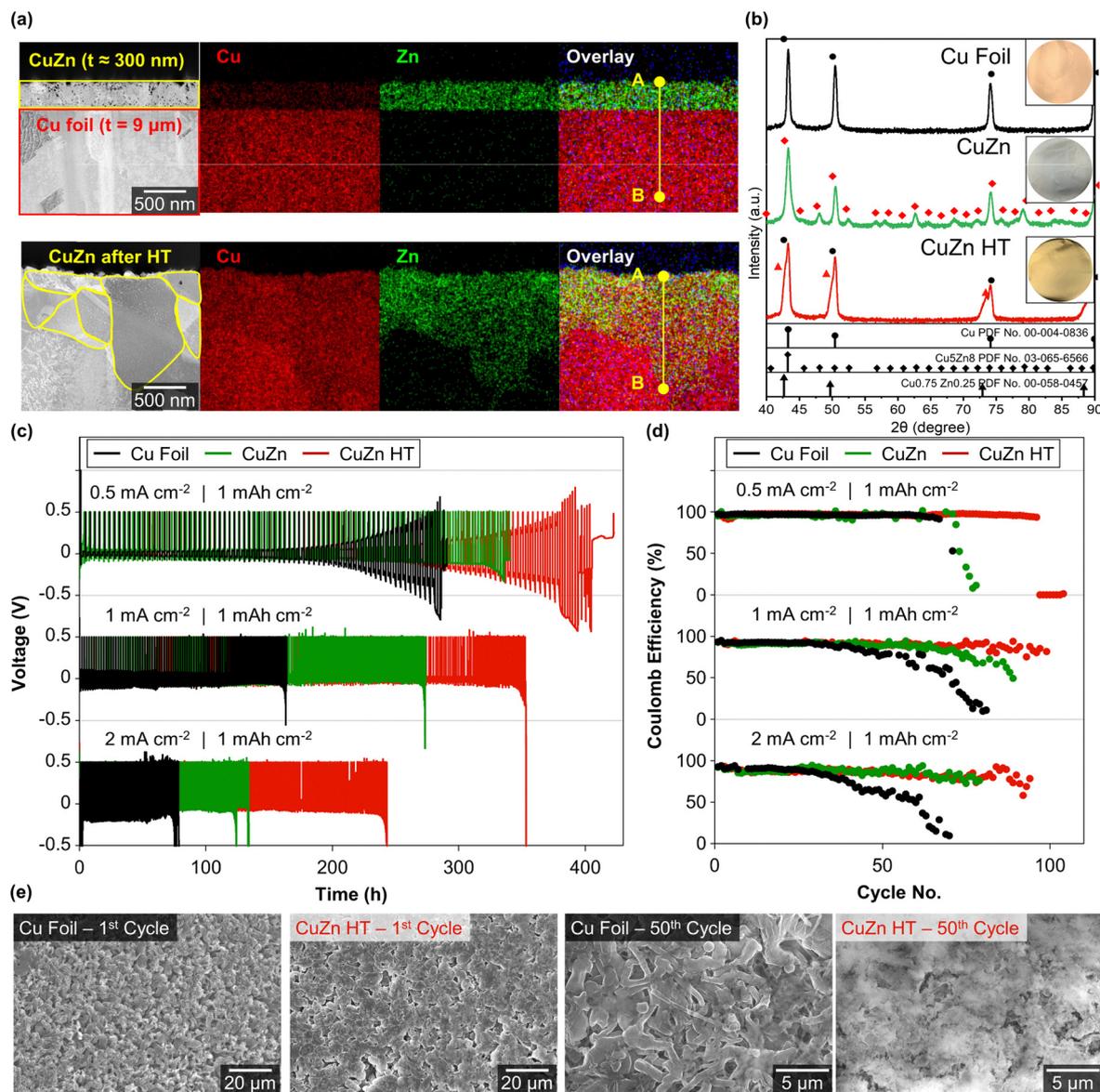
Fig. 5 Post-annealing effect on CuZn co-electrodeposited current collectors and their electrochemical performance. (a) TEM−EDS mapping images of CuZn films on Cu foil before and after post-annealing. (b) GIXRD patterns showing phase evolution from Cu_5Zn_8 to $Cu_{0.75}Zn_{0.25}$ after annealing. (c) Galvanostatic cycling performance (lifetime) of half cells measured at current densities of 0.5, 1, and 2 mA cm^{-2} with an areal capacity of 1 mAh cm^{-2}. (d) Coulombic efficiency (CE) trends under the same current densities, demonstrating improved Li reversibility and cycling stability after surface modification and thermal treatment. (e) SEM images of Li deposition morphology after the 1st and 50th Li plating cycles (following five formation cycles).

electrochemical comparison, followed by quantitative structural and compositional analysis.

Galvanostatic charge–discharge (GCD) cycling tests were performed on both nano-CuZn electrodes at a current density of 0.5 mA cm^{-2} with an areal capacity of 1 mAh cm^{-2}. As shown in Fig. 6a, the nano-$Cu_{10}Zn_{40}$ electrode exhibited a 32.4% longer lifespan compared to the nano-$Cu_{20}Zn_{30}$ current collector. Additionally, the number of cycles maintaining a Coulombic efficiency (CE) above 80% increased from 101 cycles for $Cu_{20}Zn_{30}$ to 133 cycles for $Cu_{10}Zn_{40}$ (Fig. 6b).

The branch size and density of nano-CuZn significantly influence lithium deposition behavior during cycling. Therefore, we analyzed how variations in the Cu^{2+}/Zn^{2+} ratio in the

electrolyte determine the resulting CuZn surface morphology and how these structural differences affect cycling stability. The surface morphology and density of the nanostructures were characterized by atomic force microscopy (AFM, Nanosurf), as shown in Fig. 6c. The surface roughness (S_q) was measured to be 0.35 μm for the sparser nano-$Cu_{10}Zn_{40}$ structure and 0.44 μm for the relatively denser nano-$Cu20Zn30$ structure.

Nanobranch geometry varied markedly depending on the Cu^{2+}/Zn^{2+} ratio and ion supply conditions. Under identical deposition conditions (800 mM PP, 3 V, and 2 min), increasing the Cu concentration from $Cu_{10}Zn_{40}$ to $Cu_{20}Zn_{30}$ produced shorter but significantly denser nanobranches. As shown in Fig. 6d, quantitative structural parameters were extracted from
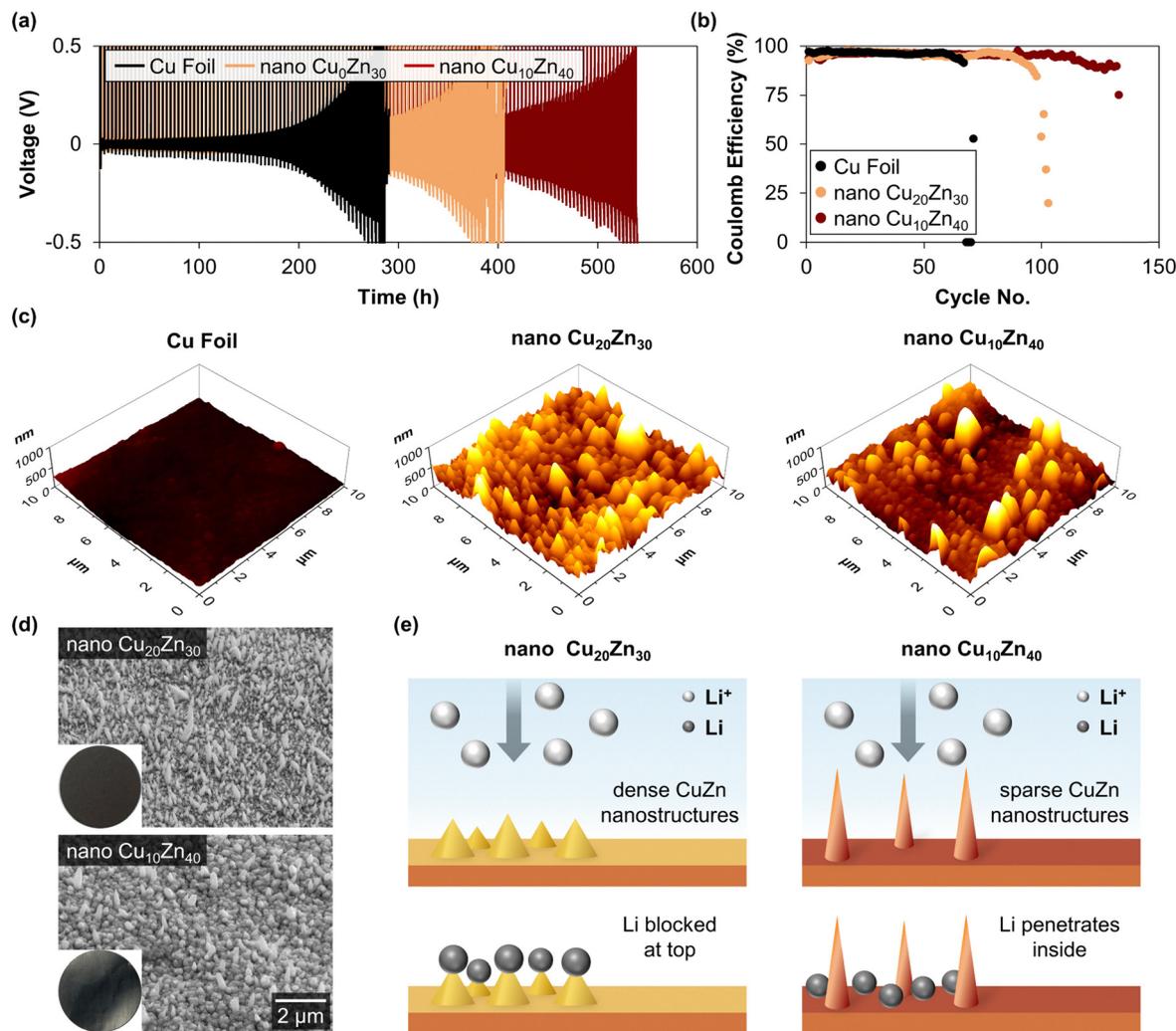
Fig. 6 Comparative analysis of the electrochemical and morphological properties of Cu foil, nano-$Cu_{20}Zn_{30}$, and nano-$Cu_{10}Zn_{40}$ current collectors. (a) GCD cycling results show a longer lifespan of nano-$Cu_{10}Zn_{40}$, attributed to its improved surface structure. (b) Coulombic efficiency trends indicate enhanced Li reversibility in denser nanostructures. (c) AFM images reveal a higher nanostructure density in nano-$Cu_{20}Zn_{30}$ compared to nano-$Cu_{10}Zn_{40}$. (d) SEM images of nano-CuZn current collectors electrodeposited at different Cu^{2+}/Zn^{2+} ratios under identical conditions (800 mM PP, 3 V, and 2 min). (e) Schematic illustration of Li plating behavior, showing localized top plating in rougher structures and more uniform deposition on denser surfaces.

SEM image analysis, including branch diameter, height, surface coverage density, and top-surface area. The $Cu_{20}Zn_{30}$ structure exhibited an average branch diameter of 177 nm and a height of 587 nm, corresponding to a 37% increase in diameter and a 76% reduction in height compared with $Cu_{10}Zn_{40}$. In addition, the nanostructure density increased by approximately 2.4-fold, while the top-surface area decreased by 62%, resulting in a characteristic short-and-dense nanobranch morphology. Notably, since the deposition current density and time were identical for both samples, the total transferred charge and thus the overall amount of deposited CuZn was comparable. Therefore, the denser $Cu_{20}Zn_{30}$ structure consisted of numerous shorter branches, whereas the relatively sparse $Cu_{10}Zn_{40}$ structure developed fewer but longer nanobranches. EDS analysis confirmed a Zn-lean composition (65.9% Cu and 34.1% Zn) of $Cu_{20}Zn_{30}$, consistent with the higher Cu fraction in the electrolyte. The increased branch density is attributed to enhanced Cu^{2+} reduction kinetics at higher Cu concentration, which promotes more frequent nucleation events and consequently leads to a greater number of closely spaced nanobranches.

The difference in electrochemical performance is attributed to variations in electric field distribution induced by nanostructure density (Fig. 6e). Densely packed nanostructures tend to concentrate the electric field at the tips of adjacent branches, promoting localized lithium deposition. This top-dominant deposition pattern (top plating) limits effective utilization of the inter-branch surface area and can reduce lithium plating efficiency. In contrast, the relatively lower nanobranch density in nano-$Cu_{10}Zn_{40}$ allows more uniform electric field distribution and improved lithium accessibility between branches, resulting in more homogeneous lithium deposition and enhanced cycling stability. These results demonstrate that tuning the Cu^{2+}/Zn^{2+} ratio in the electrolyte effectively controls

nanostructure density, which in turn governs electric field distribution and lithium deposition behavior.

3.5 Electrochemical analysis of co-electrodeposited CuZn current collectors

Electrochemical impedance spectroscopy (EIS) was conducted to quantify the interfacial characteristics of the nanostructured CuZn current collector. As shown in Fig. 7a, two semicircles corresponding to two distinct time constants were observed in the Nyquist plots of the CuZn HT and nano-CuZn electrodes. This behavior indicates the presence of two different resistive components at the electrode/electrolyte interface. In this study, the first semicircle in the high-frequency region was assigned to the surface film/SEI-related resistance, while the second semicircle in the mid-frequency region was attributed to the charge-transfer resistance (R_{ct}). Each resistance component was quantified separately (Fig. 7b).

CuZn HT exhibited reductions in both resistance components and showed the lowest total interfacial resistance. In contrast, nano-CuZn showed a reduced first semicircle (surface film/SEI resistance) but a relatively increased second semicircle (charge-transfer resistance), resulting in a slightly higher total interfacial resistance than that of CuZn HT. This trend suggests that the introduction of Zn promotes favorable interfacial reactions, such as improved surface film formation and wettability. At the same time, the nanostructured surface, which possesses increased roughness and enlarged effective surface area, may introduce more complex local charge-transfer pathways and non-uniform current distribution. In addition, a high surface area structure can increase the total area available for SEI formation and expand the interfacial reaction region, which may influence the charge-transfer resistance component. Despite this increase in R_{ct}, nano-CuZn effectively suppresses the initial irreversible reactions through its lower surface film resistance and enhanced lithium nucleation behavior. This interfacial stabilization contributes to the improved cycling stability observed in the subsequent full-cell tests.

Lithium nucleation behavior was evaluated from the voltage response during the initial plating stage. The nucleation overpotential reflects the energy barrier required for the formation of the first lithium nuclei on the current collector surface. A lower value indicates more uniform nucleation and a more stable initial deposition process. As shown in Fig. 7c, nano-CuZn exhibited a significantly lower nucleation overpotential than bare Cu. This result can be explained by the higher lithiophilicity of Zn and the increased number of active nucleation sites on the surface. The nano/branched morphology increases the number of available nucleation sites within a given geometric area and reduces local current concentration. As a result, lithium deposition becomes more homogeneous and less localized. The reduced nucleation overpotential observed for nano-CuZn provides favorable interfacial conditions that suppress irreversible lithium consumption and mitigate non-uniform lithium deposition during repeated cycling.
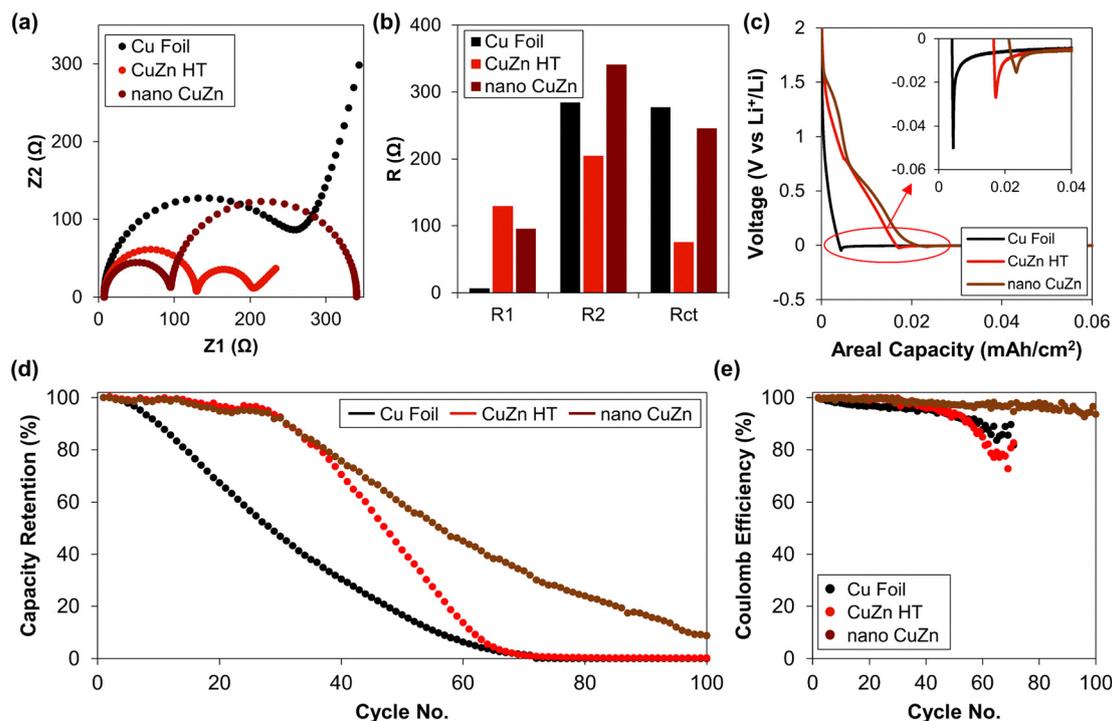

Fig. 7 Electrochemical performance comparison of Li‖Cu foil, Li‖CuZn HT, and Li‖nano-CuZn cells. (a) Electrochemical impedance spectra (EIS) showing two distinct semicircles corresponding to surface film resistance and charge-transfer resistance. (b) Quantitative comparison of surface film resistance and charge-transfer resistance for Cu foil, CuZn HT, and nano-CuZn current collectors. (c) Lithium nucleation overpotential measured during the initial plating process. (d) Cycling performance of NCM523 full cells assembled with pre-deposited Li on Cu foil, CuZn HT, and nano-CuZn current collectors. (e) Coulombic efficiency of the corresponding full cells during cycling.

A full-cell test was conducted using three current collectors: bare Cu foil, a heat-treated CuZn-coated current collector (CuZn HT) prepared by film-type coating at 2 V for 2 min from a $Cu_{10}Zn_{40}PP_{100}$ bath, and a nanostructured CuZn current collector (nano-CuZn) prepared at 3 V for 2 min from a $Cu_{10}Zn_{40}PP_{800}$ bath. The cathode was single-sided NCM523 (Ni : Co : Mn = 5 : 2 : 3, MTI Corp.) with an areal capacity of 1.774 mAh cm^{-2}. Li was pre-deposited onto each current collector to achieve an N/P ratio of 1.8 (3.193 mAh cm^{-2}). After Li pre-deposition, the coin cell was disassembled and reassembled into a full cell by replacing the Li chip with an NCM523 cathode.

For cycling, cells were rested for 5 h and then subjected to two formation cycles at 0.05C within 3.0–4.2 V, followed by regular cycling at 0.2C. Based on an 80% capacity retention criterion, the cycle life was 15 cycles for bare Cu, 37 cycles for CuZn HT, and 38 cycles for nano-CuZn (Fig. 7d). Thus, the introduction of Zn increased the early-stage lifetime (80% retention) by approximately 140%. This result indicates that Zn effectively reduces the initial irreversible capacity loss. When the cycle life was evaluated based on 20% capacity retention, CuZn HT and nano-CuZn exhibited 58 and 86 cycles, respectively. These results show that the nanostructured CuZn current collector provides superior stability during the later stages of cycling. For both Cu foil and CuZn HT, the Coulombic efficiency dropped below 90% at approximately 56 cycles. In contrast, nano-CuZn maintained a Coulombic efficiency above 90% for more than 100 cycles (Fig. 7e). This behavior confirms that nano-CuZn more effectively suppresses irreversible lithium consumption during repeated cycling.

4. Conclusion

In this study, we developed a scalable and tunable CuZn co-electrodeposition strategy to fabricate lithiophilic and structurally robust current collectors for lithium–metal batteries. By incorporating potassium pyrophosphate as a complexing agent, the reduction potential of Cu^{2+} was modulated to enable concurrent deposition with Zn^{2+} in a single bath. The resulting CuZn layers exhibited controlled morphologies ranging from compact films to high-surface-area branched nanostructures through simple adjustment of metal ion concentrations and deposition voltages. Post-annealing promoted interfacial recrystallization and the formation of a $Cu_{0.75}Zn_{0.25}$ alloy phase, which improved adhesion and mitigated delamination. Compared to bare Cu foils, the heat-treated CuZn current collector extended the cell lifespan by 44.3% and improved Coulombic efficiency retention. Further enhancement was achieved through nanostructured surface engineering, with the nano-CuZn current collector reducing interfacial resistance by 65.2% and Li nucleation overpotential by 79.5%, resulting in a total lifespan improvement of 87.2%. Moreover, systematic tuning of Cu^{2+}/Zn^{2+} ratios demonstrated that the nano-$Cu_{10}Zn_{40}$ composition delivered the best performance, extending the number of stable cycles (CE > 80%) by 32.4% over the nano-$Cu_{20}Zn_{30}$ variant. This improvement is attributed to the denser surface

morphology and more favorable electric field distribution, which enabled uniform and conformal lithium plating. Collectively, this work establishes CuZn co-electrodeposition, combined with thermal treatment and nanostructuring, as a practical and industrially compatible route to improving the stability and efficiency of lithium–metal anodes. The compatibility of this approach with roll-to-roll processing highlights its strong potential for integration into next-generation high-energy-density battery manufacturing platforms.

Conflicts of interest

There are no conflicts to declare.

Data availability

The data that support the findings of this study are available from the corresponding author upon reasonable request.

Acknowledgements

References

1 H. Wang, C. Wang and Y. Tang, *EcoMat*, 2021, **3**, e12172.
2 D. Lin, Y. Liu and Y. Cui, *Nat. Nanotechnol.*, 2017, **12**, 194–206.
3 Y. Liu, Y. Li, J. Sun, Z. Du, X. Hu, J. Bi, C. Liu, W. Ai and Q. Yan, *Nano Res. Energy*, 2023, **2**, e9120048.
4 A. Pei, G. Zheng, F. Shi, Y. Li and Y. Cui, *Nano Lett.*, 2017, **17**, 1132–1139.
5 D. Lin, Y. Liu, Y. Li, Y. Li, A. Pei, J. Xie, W. Huang and Y. Cui, *Nat. Chem.*, 2019, **11**, 382–389.
6 P. Li, C. Li, Y. Yang, C. Zhang, R. Wang, Y. Liu, Y. Wang, J. Luo, X. Dong and Y. Xia, *Research*, 2019, 2019.
7 X. Cao, P. Gao, X. Ren, L. Zou, M. Engelhard, B. Matthews, J. Hu, C. Niu, D. Liu, B. Arey, C. Wang, J. Xiao, J. Liu, W. Xu and J. Zhang, *Proc. Natl. Acad. Sci. U. S. A.*, 2021, **118**, e2020357118.
8 Y. Zhao, T. Zhou, T. Ashirov, M. El Kazzi, C. Cancellieri, L. Jeurgens, J. Choi and A. Coskun, *Nat. Commun.*, 2022, **13**, 2575.
9 T. Yang, Y. Sun, T. Qian, J. Liu, X. Liu, F. Rosei and C. Yan, *Energy Storage Mater.*, 2020, **26**, 385–390.
10 M. Tikekar, S. Choudhury, Z. Tu and L. Archer, *Nat. Energy*, 2016, **1**, 1–7.
11 Q. Wang, J. Yang, Z. Wang, L. Shi, Y. Zhao and S. Yuan, *Energy Technol.*, 2020, **8**, 1901429.
12 T. Wang, X. Liu, Y. Wang and L. Fan, *Adv. Funct. Mater.*, 2021, **31**, 2001973.
13 T. Wang, D. Zhao, K. Liang and Y. Li, *Nano Res.*, 2024, **17**, 8706–8728.

14 M. Gong, R. Yu, C. Zhou, Y. Yu, Q. Pan, C. Dong, C. Shen, Y. Guan, C. Sun, L. Mai and X. Xu, *ACS Nano*, 2024, **18**, 20648–20658.

15 H. Li, G. Wang, J. Hu, J. Li, J. Huang and S. Xu, *Energy Environ. Mater.*, 2024, **7**, e12768.

16 J. Zhang, Y. Chang, J. Yu, Y. Wang, Z. Huang, M. Yao, Z. Jiang, G. Xie and J. Qu, *ACS Appl. Mater. Interfaces*, 2024, **16**, 42332–42342.

17 I. Yang, J. Jeong, J. Seok and S. Kim, *Adv. Energy Mater.*, 2023, **13**, 2202321.

18 N. Li, J. Zhao, Z. Long, R. Song, Y. Cui, J. Lin, H. Xu and Y. Huang, *Adv. Funct. Mater.*, 2024, **34**, 2316582.

19 S. Liu, X. Zhang, R. Li, L. Gao and J. Luo, *Energy Storage Mater.*, 2018, **14**, 143–148.

20 N. Zhang, S. Yu and H. Abruna, *Nano Res.*, 2020, **13**, 45–51.

21 Y. Fang, Y. Hsieh, M. Khosravifar, K. Johnson, P. Adusei, S. Kanakaraj, S. Preisler, G. Zhang and V. Shanov, *Mater. Sci. Eng., B*, 2021, **267**, 115067.

22 Y. Guo, H. Li and T. Zhai, *Adv. Mater.*, 2017, **29**, 1700007.

23 D. Zhang, A. Dai, B. Fan, Y. Li, K. Shen, T. Xiao, G. Hou, H. Cao, X. Tao and Y. Tang, *ACS Appl. Mater. Interfaces*, 2020, **12**, 31542–31551.

24 C. Yang, Y. Yin, S. Zhang, N. Li and Y. Guo, *Nat. Commun.*, 2015, **6**, 8058.

25 K. Chen, A. Sanchez, E. Kazyak, A. Davis and N. Dasgupta, *Adv. Energy Mater.*, 2019, **9**, 1802534.

26 C. Schneider, W. Rasband and K. Eliceiri, *Nat. Methods*, 2012, **9**, 671–675.

27 A. Varzi, L. Mattarozzi, S. Cattarin, P. Guerriero and S. Passerini, *Adv. Energy Mater.*, 2018, **8**, 1701706.

28 E. Mkawi, K. Ibrahim, M. Ali, M. Farrukh, A. Mohamed and N. Allam, *J. Electroanal. Chem.*, 2014, **735**, 129–135.

29 S. Vivegnis, J. Delhalle, Z. Mekhalif and F. Renner, *Electrochim. Acta*, 2019, **319**, 400–409.

30 J. Yang, L. Chen, D. Wu, Q. Zuo, H. Chen and Q. Nie, *Appl. Surf. Sci.*, 2025, **679**, 161229.

31 M. Zaki, K. Nouneh, M. Touhami, R. Belakhmima, A. Galca, L. Pintilie, M. Enculescu, M. Baibarac and M. Taibi, *Opt. Mater.*, 2018, **83**, 252–256.

32 F. Ferreira, F. Silva, A. Luna, D. Lago and L. Senna, *J. Appl. Electrochem.*, 2007, **37**, 473–481.

33 S. Vivegnis, M. Krid, J. Delhalle, Z. Mekhalif and F. Renner, *J. Electroanal. Chem.*, 2019, **848**, 113310.

34 A. Yavuz, M. Haciibrahimoglu and M. Bedir, *Mater. Res. Express*, 2018, **5**, 016401.

35 J. Zhao, L. Sun, S. Canepa, H. Sun, M. Yesibolati, M. Sherburne, R. Xu, T. Sritharan, J. Loo, J. Ager, J. Barber, K. Molhave and Z. Xu, *J. Mater. Chem. A*, 2017, **5**, 11905–11916.